Second harmonic spectroscopy of ZnO, BiFeO 3 and LiNbO 3 nanocrystals

Jérémy Riporto, Mathias Urbain, Yannick Mugnier, Volodymyr Multian, Florian Riporto, Kévin Bredillet, Sandrine Beauquis, Christine Galez, Virginie Monnier, Yann Chevolot, et al.

Second harmonic spectroscopy of ZnO, $BiFeO_3$ and $LiNbO_3$ nanocrystals

Jérémy Riporto[1,2], Mathias Urbain[1], Yannick Mugnier[1], Volodymyr Multian[1,3], Florian Riporto[1], Kévin Bredillet[1], Sandrine Beauquis[1], Christine Galez[1], Virginie Monnier[4], Yann Chevolot[4], Volodymyr Gayvoronsky[3], Luigi Bonacina[2], Ronan Le Dantec[1*]

[1] *Univ. Savoie Mont Blanc, SYMME, F-74000 Annecy, France*
[2] *Department of Applied Physics, Université de Genève, 22 chemin de Pinchat, 1211 Genève 4, Switzerland*
[3] *Institute of Physics NAS of Ukraine, pr.Nauki 46, Kyiv 03680, Ukraine*
[4] *Université de Lyon, Ecole Centrale de Lyon, UMR CNRS 5270, Institut des Nanotechnologies de Lyon (INL), F-69134 Ecully, France*
*ronan.le-dantec@univ-savoie.fr

Abstract: We developed a wavelength-tunable second harmonic scattering experimental setup to investigate dispersion of the nonlinear optical response of three different nanocrystal suspensions ($LiNbO_3$, ZnO and $BiFeO_3$). Special attention was paid to reproducibility issues with the implementation of a detailed protocol that allows correcting for the setup spectral response. The absolute, orientation-averaged second order susceptibilities of the three nanomaterials were then assessed in the 700-1300 nm spectral range evidencing very specific optical signatures. The well-defined resonances observed for ZnO and $BiFeO_3$ near their electronic transitions were found to be poorly described by the Miller's rule.

1. Introduction

Nonlinear optical frequency conversion in nanocrystals and nanostructures provides coherent and widely tunable signals for applications in various fields such as nanophotonic systems and bio-imaging. The intensity of the emitted harmonics is reduced at the nanoscale so that different strategies, mostly based on optically resonant structures, have recently emerged to compensate for this scale law. For instance, metal-based nanostructures [1-3] and Mie-resonant nanoparticles [4-6] evidence strong enhancements of the nonlinear optical effects and offer very appealing perspectives in terms of improved conversion efficiency. Nonlinear optical spectroscopy has thus become essential in order to accurately assess the magnitude of these frequency-dependent enhancements. In addition to nanostructures, the study of the intrinsic nonlinear response of bare nanocrystals is also of great importance to better quantify and understand the above mentioned resonances. Regarding bulk crystals, the wavelength-dependence of their nonlinear susceptibilities have been scarcely studied and data are often limited to discrete wavelengths [7] due to the lack in the past of readily available tunable excitation sources and because of material transparency issues. Among spectrally resolved Second Harmonic (SH) studies, an increase in the susceptibility has been demonstrated so far for zinc-blende II-VI semiconductors [8], GaAs [9] and ZnO [10,11] when the SH frequency is tuned to the electronic transition energies. These studies provide experimental data for comparison with theoretical models which still need to be refined.

To this end, we here report on the development of a tunable Hyper Rayleigh Scattering (HRS) setup to quantitatively access the orientation-averaged second-order susceptibility $\langle\chi^{(2)}\rangle$ of three different Harmonic Nanoparticles (HNPs), namely Zinc Oxide (ZnO), Bismuth Ferrite ($BiFeO_3$ or BFO) and Lithium Niobate ($LiNbO_3$ or LN). HNPs are inorganic oxide nanocrystals displaying a very rich nonlinear response because of their non-centrosymmetric

crystal structure. Both even and odd harmonics originate from the nanocrystal volume (when its size is typically above 10-20 nm) and among the different accessible nonlinear processes, SH generation has already proven to be very useful in bio-imaging because of unique properties including coherent and narrow spectral emissions, excitation wavelength tunability, and photostability [12-14]. When HNPs are used as exogenous optical contrast agents, sensitivity and selectivity can also be increased when the second- and third-order signals are simultaneously collected in demanding imaging applications [15,16].

Contrary to individual nanocrystal imaging, ensemble measurements from HRS are more prone to give quantitative information as initially demonstrated with the determination of molecular hyperpolarizabilities [17]. This technique has later been extended to probe the second harmonic scattering (SHS) of larger objects such as metallic nanoparticles [18], quantum dots [19] and biological structures [20]. SHS spectroscopy from ensemble measurements was then first developed by Campo et *al*. [21] ten years ago with the design of a widely tunable (excitation from 600 to 1800 nm) HRS set-up to study the hyperpolarizability dispersion of various molecules [22-23]. So far, SH spectroscopy from individual nanocrystals and nanostructures was only carried out in multiphoton microscopy [24-25] with the severe limitation that calibration of the focusing and collection parameters from diffraction-limited objects is not trivial, especially because the intensity at 2ω strongly depends on the nanocrystal orientation [26]. SHS spectroscopy from colloidal nanocrystal suspensions is here developed from a recent tunable commercial source.

This article is organized as follows: after a description of the experimental setup and theoretical background in section 2, calibration is detailed in section 3.1 from suspensions of LN nanocrystals. The relative, orientation-averaged susceptibility of LN is first calibrated against chloroform and compared with literature values of bulk crystals. Rescaling in the full excitation range is then derived from the well-known response of para-nitroaniline molecules at 1064 nm. In section 3.2 and 3.3, SHS spectroscopy is applied to ZnO and BFO suspensions to quantitatively assess their orientation-averaged second-order susceptibility. Validity of the calibration procedure and the wavelength-dependence of the absolute susceptibilities are finally discussed in section 4.

2. Experimental procedures and data analysis

As illustrated in Fig.1, SHS spectroscopy is here based on a widely tunable (680 to 1300 nm) femtosecond laser (Insight X3 Spectra-Physics). The incident power is controlled thanks to an achromatic half-wave plate (Thorlabs, 690-1200 nm) associated with a vertical Glan-laser polarizer (Thorlabs). A near-infrared achromatic lens (Newport, f = 100 mm) mounted on a motorized translation stage is placed after a long pass filter (Thorlabs FELH0650) and is used to focus the incident beam at the center of a UV-fused quartz cuvette filled with the nanocrystal suspensions. The second harmonic signal is collected perpendicularly to the laser beam through two fused silica lenses (Thorlabs, f = 50 mm). An uncoated BK7 Dove prism (Thorlabs) is inserted between these two lenses so as to rotate the (horizontal) focal point image and to increase the signal [27] on the vertical entrance slit of a spectrometer (Andor Shamrock 193) coupled to a Peltier-cooled CCD camera (Andor iDus 401). A short pass filter is also placed in front of the spectrometer to remove scattering of the fundamental beam. This short pass filter is either composed of two FGB37 Thorlabs colored glass filters in the 700-800 nm excitation range or a single Thorlabs FESH0700 filter in the 800-1300 nm range. Full automation of the whole set-up ensures reproducible experimental conditions and allows scanning the excitation wavelength during a spectroscopic measurement. At each wavelength, the incident power is set to the required value and the dispersion pre-compensation is optimized to keep constant the pulse width within the sample. For an incident power of 500 mW, the wavelength-independent intensity at the focal point is calculated at 1 GW/cm^2 and a typical 1 min integration time is then necessary to collect the SHS spectra at each excitation

wavelength. In case of residual background or multiphoton photoluminescence, a multi-peak fitting procedure was also implemented to only assess the SH signal.

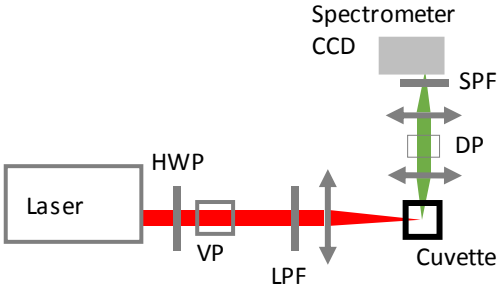

Fig. 1: Sketch of the SHS spectroscopy setup. HWP: achromatic Half-Wave Plate, VP: Vertical Glan-laser Polarizer, LPF: Long Pass Filter, DP: uncoated BK7 Dove Prism and SPF: Short Pass Filter.

In previous works, we have adapted the HRS technique to measure at 1064 nm the orientation-averaged second-order susceptibility of several harmonic nanoparticles [12,28,29]. In the following, the formalism at a single excitation wavelength is briefly reminded. The second harmonic signal scattered by a nanoparticle (np) suspension (neglecting the solvent contribution) can be expressed as:

$$I_{2\omega} = G\, N_{np} \left(t_{\omega}^{4} t_{2\omega}^{2} \right)_{np} \left\langle \beta_{eff}^{2} \right\rangle I_{\omega}^{2} \qquad (1)$$

G includes experimental parameters and fundamental constants related to the electric dipole radiation, N_{np} is the concentration of nanoparticles and I_{ω} the incident intensity. The macroscopic internal field factor that is calculated at the fundamental and SH frequencies is defined at ω as:

$$t_{\omega} = 3(n_{\omega}^{s})^{2} \Big/ \left(2(n_{\omega}^{s})^{2} + (n_{\omega}^{np})^{2} \right) \qquad (2)$$

for a spherical nanoparticle [30] with n_{ω}^{s} and n_{ω}^{np} the refractive indexes of the solvent and nanoparticle, respectively. $\langle \beta_{eff}^{2} \rangle$ is the effective squared hyperpolarizability averaged over all possible orientations. The term "effective" is here introduced to account for the volume-dependent response of the nanocrystal (SH fields radiated from each crystal cell build up coherently within the dipolar approximation) and to make a clear distinction with the usual (microscopic) molecular hyperpolarizability. The orientation-averaged second-order susceptibility $\langle \chi^{(2)} \rangle$ is then calculated from the effective hyperpolarizability and nanoparticle volume V_{np} as [28]:

$$\left\langle \chi^{(2)} \right\rangle = 2 \left\langle \beta_{eff} \right\rangle \Big/ V_{np} \qquad (3)$$

In practice, quantitative information can only be derived after calibration of the experimental setup. Herein, the external reference method is applied with para-nitroaniline (pNA) molecules dissolved in methanol. Neglecting again the solvent contribution, the unknown experimental constant *G* of eq. 1 can be removed since the HRS signal from a pNA solution is given by:

$$I_{2\omega} = G\, N_{pNA} \left(f_{\omega}^{4} f_{2\omega}^{2} \right)_{pNA} \left\langle \beta_{pNA}^{2} \right\rangle I_{\omega}^{2} \qquad (4)$$

where f_ω and $f_{2\omega}$ are the usual Lorentz-Lorenz field factors and $\langle\beta_{pNA}\rangle = (6/35)^{1/2}\ \beta_{33}$ (β_{33}=25.9.10^{-30} at 1064 nm [31]). After plotting $I_{2\omega}$ as a function of the pNA concentration and of the concentration of nanoparticles, $\langle\beta_{eff}\rangle$ is then obtained from the ratio of the two corresponding slopes. Note that N_{np} is estimated by weighing the residual powder after evaporation of the suspension used in the SHS measurements. The average nanoparticle volume is also determined within the suspension by using Dynamic Light Scattering (DLS) so that $\langle\chi^{(2)}\rangle$ can be finally calculated from eq. 3. The experimental protocol, applied conventions and different limitations of this technique are detailed in ref. [29] which describes the same experiments at a constant 1064 nm excitation wavelength.

For this work and to ensure consistency with our previous reports, we have applied this protocol to retrieve the absolute $\langle\chi^{(2)}\rangle$ values of the different HNPs at 1064 nm. However, pNA cannot be used on the whole spectral range as a reference since its hyperpolarizability is known exclusively at 1064 nm. The ideal reference should be transparent at the fundamental and second harmonic frequencies besides having a high non-resonant nonlinear susceptibility and limited hindrance by multiphoton fluorescence. Calibration over broad excitation range is thus a major issue. In ref. [21], the dispersion of a large range of solvent has been measured against chloroform. Considering its transparency range and non-resonant response, chloroform was here first used as a reference to evaluate dispersion of the $LiNbO_3$ second-order susceptibility that was found in good agreement with literature values. Lithium niobate nanocrystal suspensions are then employed as a new external reference material to better match with the above criteria because of the large material transparency range, the scattering of strong SH signals and the absence of any stray luminescence.

3. Results

3.1 SHS spectroscopy of $LiNbO_3$ suspensions

Lithium niobate is a well-known ferroelectric material with high and well-characterized SH coefficients [7]. Regarding nanoparticle suspensions with low size and shape polydispersity, they can be prepared by using the solvothermal approach developed by Mohanty et al [32]. Well-crystallized and phase-pure $LiNbO_3$ nanoparticles were thus obtained with an average size at ~50 nm as imaged by Transmission Electron Microscopy (Fig. 2). When dispersed in Ethanol, suspensions are very stable and show a very low polydispersity with a typical mean diameter measured at about 70 nm from DLS measurements.

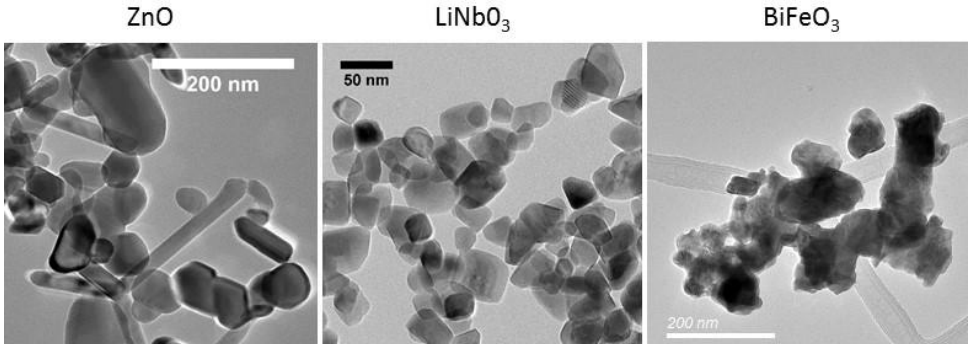

Fig. 2. Representative TEM images of ZnO, $LiNbO_3$ and $BiFeO_3$ samples

As previously introduced, the calibration protocol is based on a two-step procedure with first, the determination of a relative value of the frequency-dependent susceptibility $\langle\chi^{(2)}\rangle_{Rel}^{LN}$ of LN. This relative value is derived from eq. 5 as detailed below after the successive acquisition of the SHS signal $I_{LN}(\lambda)$ from a LN suspension and the one, $I_{chloro}(\lambda)$ from a

chloroform solution by varying the excitation wavelength. The absolute value $\langle \chi^{(2)} \rangle_{1064}^{LN}$ is then determined at 1064 nm from the reference solution of pNA molecules dissolved in methanol. Finally, the absolute value of the orientation-averaged susceptibility of LN is rescaled in the full spectral range. Fig. 3 illustrates typical emission spectra for both LN suspensions and chloroform obtained from a constant power set at 500 mW, *i.e* an incident intensity at 1 GW/cm^2. Only pure SH scattering is observed for LN suspensions in ethanol while chloroform spectra show an additional, small red-shifted peak associated to a hyper-Raman scattering band [33]. Note also that the SH signal from chloroform is very low comparatively to LN suspensions and that the integration time had to be increased to 5 minutes. In spite of the lower response of chloroform, the relative susceptibility of LN could be derived from the measured SH intensities and by using the following relationship deduced form eq. 1 and eq. 4 in the case of a chloroform solution:

$$\left\langle \chi^{(2)}(\lambda) \right\rangle_{Rel}^{LN} \propto \left\langle \beta(\lambda) \right\rangle_{Rel}^{LN} \propto \sqrt{\frac{I_{LN}(\lambda)}{I_{chloro}(\lambda)} \frac{\left(f_\omega^4 f_{2\omega}^2 \right)_{chloro}(\lambda)}{\left(t_\omega^4 t_{2\omega}^2 \right)_{LN}(\lambda)}} \left\langle \beta_{chloro}(\lambda) \right\rangle \quad (5)$$

Dispersion of the chloroform hyperpolarizability $\langle \beta_{chloro}(\lambda) \rangle$ was taken from reference [21] and field factors f_ω and t_ω were calculated at the fundamental and SH frequencies from the refractive indexes of chloroform, ethanol [34] and LN [35]. The resulting relative, orientation-averaged susceptibility of LN is depicted in Fig. 3.b and shows a non-resonant response as expected for lithium niobate nanocrystals.

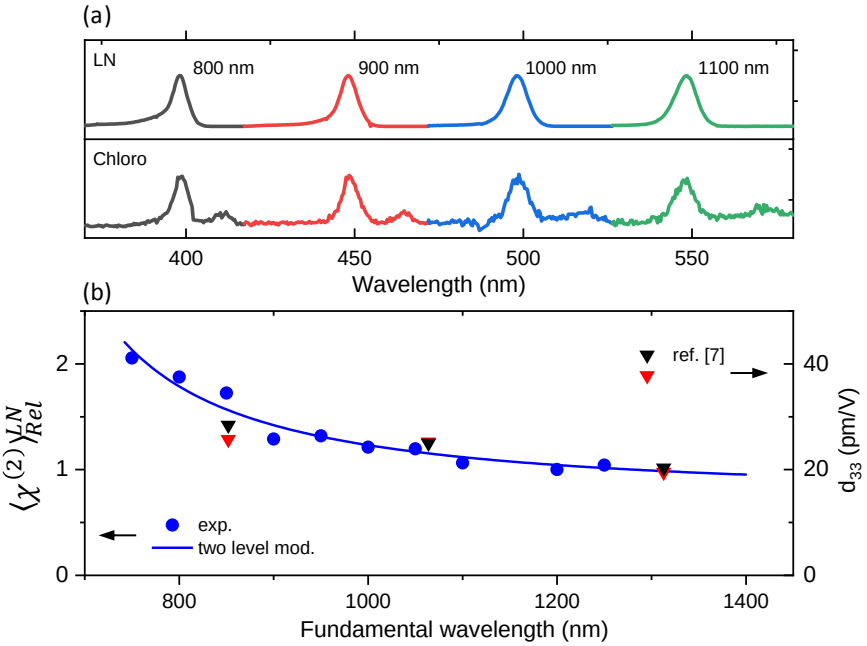

Fig. 3. (a) Representative scattering spectra from chloroform and LN suspensions in ethanol. (b) The relative, orientation-averaged susceptibility of LN (blue circle, normalized at λ=1200 nm) is compared to the d_{33} coefficient measured in ref. [7] (red triangle for congruent $LiNbO_3$ and black triangle for 5%MgO:$LiNbO_3$). Note that the left and right scales are proportional to make relevant the comparison. The blue line is a fit with the two-level model (eq. 6) described in the text.

Comparison between $\langle\chi^{(2)}\rangle_{Rel}^{LN}$ of LN and its absolute nonlinear optical coefficient $d_{33}(=\chi_{33}/2)$ measured at three discrete wavelengths by Shoji *et al.* [7] is also shown in Fig. 3b. It is worth to mention that the orientation-averaged susceptibility of LN is given in Table 1 according to the individual components of its susceptibility tensor and that the contribution of the d_{33} coefficient is the predominant one according to literature values [7,36]. Comparison between d_{33} and $\langle\chi^{(2)}\rangle_{Rel}^{LN}$ is thus relevant. Therefore, the measured susceptibility frequency dispersion from a LN colloidal suspension is found in good agreement with bulk crystal values, which is consistent with the already demonstrated absence of any size effect for the SH response of various inorganic nanocrystals in this size range [29,37]. In Fig. 3b, experimental values were also fitted with a simple two-level model which is valid far from resonance conditions [38]:

$$\chi^{(2)}(2\omega,\omega,\omega)=\chi_0^{(2)}\frac{\omega_{eg}^4}{\left(\omega_{eg}^2-\omega^2\right)\left(\omega_{eg}^2-4\omega^2\right)} \qquad (6)$$

ω_{eg} stands for the electronic transition frequency, ω for the fundamental frequency and $\chi_0^{(2)}$ for the static susceptibility. ω_{eg} and $\chi_0^{(2)}$ were used as free parameters to adjust the experimental data leading to a transition wavelength of λ_{eg} = 286 nm which is close to the experimental absorption edge of LN crystals measured at 305 nm [39]. The as-obtained smooth dispersion curve is then assumed in the following sections to be representative of the relative, orientation-averaged susceptibility of LN.

Finally, the absolute value of the orientation-averaged susceptibility of LN is obtained at 1064 nm with suspensions of varying concentrations and after calibration of the SHS set-up with pNA solutions as discussed in section 2. We found an experimental value of $\langle\chi^{(2)}\rangle_{1064}^{LN}$ at *24 pm/V* that is actually very consistent with the bulk one calculated at 26 pm/V from the expression given in Table 1 and the tensor elements from literature values (d_{33}=25.2 pm/V, d_{31}=4.6pm/V [7] and d_{22}=2.3 pm/V [36]). This further supports the experimental calibration route here developed and the use of LN suspensions as an almost ideal reference because of its background-free and high non-resonant SH response. Rescaling of $\langle\chi^{(2)}\rangle_{Rel}^{LN}$ in the full excitation range is then easily achieved to derive dispersion of the absolute orientation-averaged susceptibility. Corresponding data for LN are plotted below in Fig. 5 for a direct comparison with the dispersion curves then obtained for ZnO and $BiFeO_3$ nanocrystals.

Table 1: Mean nanocrystal size and experimental values of $\langle\chi^{(2)}\rangle$ measured at 1064 nm. $\langle\chi^{(2)}\rangle$ is also given according to the individual, non-zero elements of the second-order susceptibility matrix

	D[1] (nm)	$\langle\chi^{(2)}\rangle_{1064}$ (pm/V)	Squared orientation-averaged susceptibilities from individual tensor elements[2]
LN	73	24	$\langle\chi_{LN}^{(2)}\rangle^2=\frac{6}{35}\chi_{33}^2+\frac{8}{21}\chi_{22}^2+\frac{92}{105}\chi_{31}^2+\frac{32}{105}\chi_{31}\chi_{33}$
ZnO	134	5.3	$\langle\chi_{ZnO}^{(2)}\rangle^2=\frac{6}{35}\chi_{33}^2+\frac{92}{105}\chi_{31}^2+\frac{32}{105}\chi_{31}\chi_{33}$
BFO	90	120	$\langle\chi_{BFO}^{(2)}\rangle^2=\frac{6}{35}\chi_{33}^2+\frac{8}{21}\chi_{22}^2+\frac{92}{105}\chi_{31}^2+\frac{32}{105}\chi_{31}\chi_{33}$

[1]D, mean diameter obtained from the DLS size-distribution in number. [2]Orientation-averaged susceptibilities are here expressed assuming the Kleinman's condition and for the current experimental configuration, *i.e.* a vertical input polarization and no analyzer in the detection arm.

3.2 SHS spectroscopy of ZnO suspensions

ZnO is a wide band-gap semiconductor with a non-centrosymmetric crystal structure. Comparatively to LN and BFO, SH and even third harmonic properties of ZnO films and nanostructures including nanowires and nanoparticles have already been the subject of reviews and several papers [40,41]. Nanoparticle suspensions of ZnO dispersed in ethanol were prepared from commercial nanopowders (NanoAmor Inc., commercial size 90-200 nm) as recently described [42].

SHS spectroscopy is then performed with an excitation wavelength varying from 700 to 1300 nm as shown in Fig. 4a and 4b. Above 760 nm, only the SH signal is detected whereas an additional multiphoton-excited luminescence peak centered at 377 nm gradually appears when the excitation is shifted towards shorter wavelengths. Measured spectra are thus fitted with multiple Gaussian functions to separate the SHS intensity from the band-gap photoluminescence contribution [10]. Fig. 4c shows the normalized SHS intensity ratio $I_{ZnO}(\lambda)/\ I_{LN}(\lambda)$ which is used to derive the relative susceptibility with eq. 5 (modified by substituting chloroform with LN and LN with ZnO). A strong resonance (corrected from any photoluminescence contribution) occurs at a fundamental wavelength of 750 nm with a 10-fold enhancement compared to a non-resonant excitation at 1300 nm. This resonance will be discussed later.

The orientation-averaged susceptibility is then determined as before at 1064 nm from pNA solutions and the as-obtained experimental value $\langle\chi^{(2)}\rangle_{1064}^{ZnO} = 5.3 pm/V$ is found very consistent with previous measurements carried out with the same commercial ZnO nanopowder but with a YAG laser source [28]. Afterwards, the relative susceptibility is rescaled to obtain dispersion of the absolute, orientation-averaged susceptibility of ZnO which is also plotted in Fig. 5.

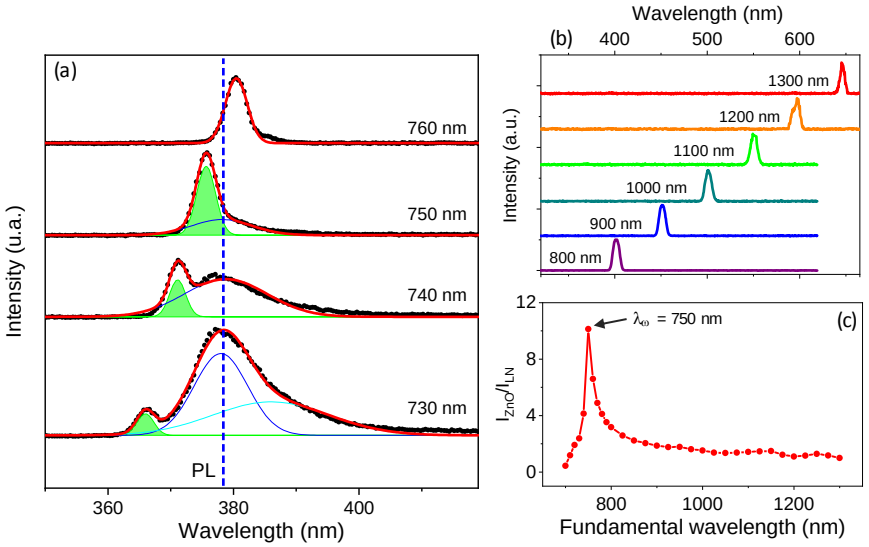

Fig. 4: (a) Two-photon scattering spectra from ZnO suspensions for an excitation wavelength below 760 nm. The two-photon absorption induces a photoluminescence peak at 377 nm that is superimposed to the SHS contribution. (b) Only the SHS signal is detected in the 760-1300 nm excitation range. (c) Experimental ratio of the SHS signals I_{ZnO} and I_{LN} from ZnO and LN

suspensions in ethanol as a function of the excitation wavelength and after normalization at λ=1300 nm. A strong resonance is observed at 750 nm.

3.3 SHS spectroscopy of $BiFeO_3$ suspensions

Bismuth Ferrite (BFO) is a promising room-temperature multiferroic material with a very high and rich nonlinear optical response. Its SH efficiency has been measured at 1064 nm and is known to vary between 158 and 440 pm/V according to the synthesis route that can yield to more or less phase-pure, monocristalline and monodisperse nanocrystals [26,43]. In this study, BFO nanoparticles were prepared through a simple co-precipitation route leading to stable BFO suspensions in ethanol with a mean typical DLS size at 90-100 nm [44]. This chelating agent-free chemical synthesis has however some drawbacks since the absence of size and morphology control has been clearly evidenced from TEM observations (Fig. 2) and a decrease of the orientation-averaged susceptibility is thus expected [29]. After preparation of a batch of BFO powders from the co-precipitation route, the same procedure previously described for ZnO is again applied for the determination of the relative and absolute orientation-averaged susceptibilities of BFO. Note that a background-free and pure SHS signal is detected over the entire excitation range (data not shown). The absolute value of $\langle \chi^{(2)} \rangle_{1064}^{BFO}$ is found to be 120 pm/V at 1064 nm, which is significantly higher than the one of LN and ZnO. The frequency-dependent orientation-averaged susceptibility of BFO is also compared in Fig. 5 with the ones of LN and ZnO nanocrystals.

4. Discussion

4.1 Validity and limitations of the calibration procedure

Because of the wide excitation range and the high number of optical parameters that should be adjusted for the whole experimental set-up, a series of sanity checks has been performed to ensure robustness of the measurement protocol. First, the SHS signal was optimized with a horizontal translation of the excitation lens and found to be maximal for each wavelength when the excitation beam is focused at the center of the sample cuvette. Interestingly, we did not observe any shift of this position in the entire excitation range thanks to the achromatic focusing lens. A well-defined and constant excitation intensity I_ω is thus maintained at the sample. Second, we confirmed that the response of the orientation-averaged susceptibility of ZnO is reproducible by varying several experimental parameters including the incident power (250 mW or 500 mW), the focal length of the excitation lens (50 mm or 100 mm) and the position of the excitation beam after shifting it from the center of the sample cuvette. In each case, the wavelength-dependent intensity ratio $I_{ZnO}(\lambda)/I_{LN}(\lambda)$ was measured and found constant. Measurement of the relative, orientation-averaged susceptibility is thus very reproducible provided that the experimental conditions are kept constant for the successive acquisition of the sample and reference data.

On the other hand, quantitative assessments of the absolute susceptibility at 1064 nm have some limitations which are detailed in ref [29]. As reminded in section 2, we indeed assume perfectly spherical nanoparticles with a narrow size-distribution and for each material, the number density of nanoparticles in suspension is supposedly known with enough accuracy. Deviations from these ideal conditions can be minimized though after reduction of the nanoparticle size- and shape-polydispersity but from our experience, the orientation-averaged susceptibility can be slightly underestimated compared to the literature values of bulk crystals. We estimate the overall experimental reproducibility of the absolute measurements at about ±15% [29].

Finally, we point out here that SHS signals are assumed to be proportional to the concentration of nanoparticles (eq. 1) but deviation may occur for highly concentrated samples, simply because of absorption and linear scattering of the fundamental and SH photons (both effects are more pronounced at the shortest wavelengths). Working in the low-

concentration regime is thus a prerequisite and ideally a series of intensity-concentration measurements should be carried out at each wavelength. To avoid these time consuming experiments, our approach consisted in repeating a second wavelength-dependence measurement of the normalized SHS intensity ratio but with a more diluted sample. For ZnO (and BFO), the ratio $I_{ZnO}(\lambda)/I_{LN}(\lambda)$ was found constant demonstrating that the the linear regime assumed in eq.1 holds for each wavelength. For the different suspensions of nanoparticles of this work, we noticed that the mass concentrations should be typically below 0,1 mg/mL and under these conditions, absorption and linear scattering of the fundamental and SH photons could not be evidenced.

4.2 Dispersion of the absolute susceptibilities

Dispersion of the absolute, orientation-averaged nonlinear susceptibility of ZnO, LN and BFO nanocrystals is plotted in Fig. 5 and from bottom to top according to their quantitative value. In the case of ZnO, the sharp resonance observed at the excitation wavelength of 750 nm ($\lambda_{2\omega}$ = 375 nm) is consistent with the exciton resonance near the bandgap [10,45]. A ~7-fold enhancement can be noticed comparatively to the off-resonance experimental value measured at ~4 pm/V. Interestingly, dispersion of the absolute susceptibility measured here is very similar to the relative frequency-dispersion obtained by Perdersen et al [10] from SHG reflection on both single crystals and nanowires. For LN, the absolute susceptibility is stronger than that of ZnO and it does not present defined resonances as already discussed. The absolute nonlinear susceptibility of BFO is well higher than the other two materials in the whole excitation range and the resonance observed at 880 nm ($\lambda_{2\omega}$ = 440 nm) is close to the BFO bandgap [46]. Noticeably, the resonance (~3-fold enhancement from the 1300 nm excitation wavelength) is less pronounced and much broader comparatively to the one of ZnO.

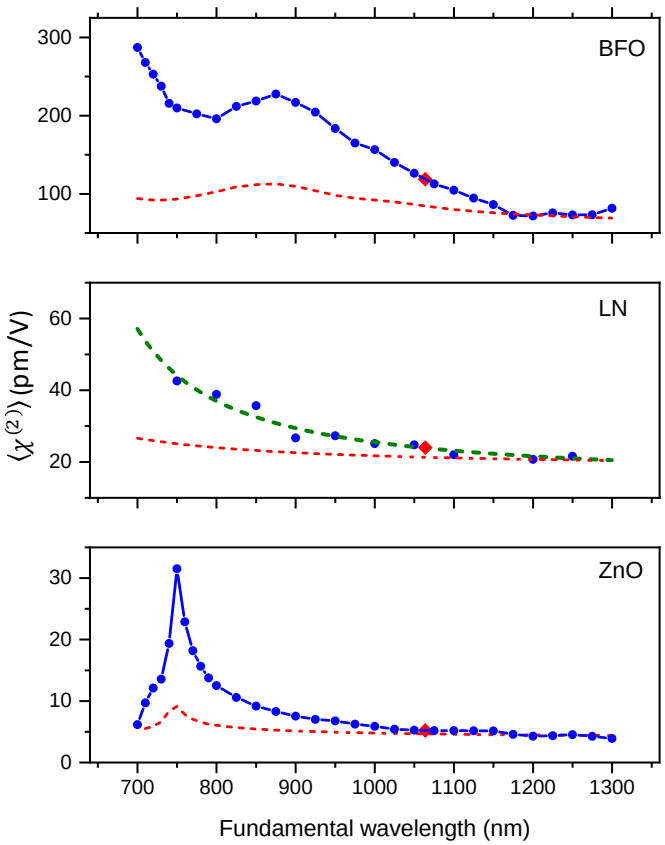

Fig. 5: Experimental absolute values of the orientation-averaged second-order susceptibility of BFO, LN and ZnO nanocrystals (blue dots). Each dispersion curve is rescaled in the 700-1300 nm excitation range from the quantitative assessment made at 1064 nm from the external reference method applied with pNA molecules dissolved in methanol (red square). For LN, the two level model is also shown (green dashed line). For each nanomaterial, the Miller's rule calculated from the linear complex susceptibility is indicated with a red dashed line.

A key point of this work is that we assume that nanoparticle nonlinear susceptibility is representative of the bulk one. Indeed, we had already verified this assumption at a fixed wavelength of 1064 nm [28, 29] and it is related to the noncentrosymmetric crystalline structure of the nanoparticles. In this framework, SH signal originates from the nanoparticle volume with negligible surface contribution [37]. The very distinct dispersion curves obtained here for the three nanomaterials are thus very similar to their bulk response. It is therefore interesting to compare these experimental dispersion curves with the empirical Miller's rule [47] stating that the ratio between the linear and non-linear susceptibilities is constant in the transparent region, *i.e.* $\chi^{(2)}(2\omega,\omega,\omega) \propto \chi^{(1)}(2\omega)\chi^{(1)}(\omega)\chi^{(1)}(\omega)$. This rule is usually applied to estimate dispersion of the nonlinear susceptibility from $\chi^{(1)}$. It was even suggested that a similar relationship still hold if the SH frequency lies in the material absorption band [48]. In the latter case, the real and imaginary parts of the linear susceptibility are to be taken into consideration to derive the nonlinear susceptibility through $\chi^{(2)}(2\omega,\omega,\omega) \propto \left|\chi^{(1)}(2\omega)\right|$ (neglecting the dispersion of $\chi^{(1)}(\omega)$ in the transparency range). We applied this approach by using the complex linear susceptibilities from the literature values of ZnO [49], LN [35] and

BFO [50], and then plotted the corresponding curves in Fig. 5. Superimposition of the experimental (blue dots) and calculated curves (dashed red line) is first fixed in the transparency region, namely 1200 – 1300 nm. As shown in Fig. 5, the estimated susceptibilities are similar in terms of shape and resonance wavelengths but this rule underestimates the amplitude of the resonance for ZnO and BFO. Notably, it does not even correctly model the experimental response of LN, which is transparent at both fundamental and second harmonic wavelengths. The validity of the Miller's rule has already been questioned [7] in the literature and more sophisticated approaches such as ab initio methods have then been developed. However, they still need refinements since the experimental $\chi^{(2)}$ dispersion is still poorly described in most cases [51]. We believe that our experimental estimations can be useful for the development of new nonlinear susceptibility models.

5- Conclusion

A new SHS spectroscopy setup was developed from an easily-operable commercial laser source. Careful attention has first been paid to the calibration and measurement protocol in the 700-1300 nm excitation range. Because of the sensibly lower HRS signals collected from typical solvents like chloroform, colloidal suspensions of LN are proposed as an appropriate choice for the external reference method. To support the use of LN suspensions, the relative orientation-averaged susceptibility of LN was first calibrated against chloroform and then compared with literature values of bulk crystals. The good agreement achieved demonstrates that LN nanocrystals are well appropriate for the calibration of SHS spectroscopy because of the high and background-free SH signals and non-resonant response of lithium niobate. This calibration route was then applied to derive dispersion of the absolute, orientation-averaged susceptibility of ZnO and BFO nanocrystals.

Distinct and specific nonlinear susceptibilities were found for each nanomaterial with resonances arising from the electronic transition near the bandgap energy for ZnO and BFO. The nanocrystal response is very similar to the bulk crystal one because SHG originates from the nanoparticle volume as previously demonstrated for an excitation wavelength at 1064 nm [29]. This experimental approach allows to quantitatively assessing the intrinsic material second order nonlinearity and can help to refine new susceptibility models besides offering a precise tool to characterize resonances of engineered nanostructures.

Funding

French-Swiss Interreg V program (project NANOFIMT), French *Agence Nationale de la Recherche* (project RACINE), French *Contrat Plan État Région* (project E-TIME).

Acknowledgements

The authors thank the CLYM platform for access to TEM equipment

References

1. M. Kauranen and A. V. Zayats, "Nonlinear plasmonics," Nat Photon **6**(11), 737–748 (2012).
2. Y. Pu, R. Grange, C.-L. Hsieh, and D. Psaltis, "Nonlinear Optical Properties of Core-Shell Nanocavities for Enhanced Second-Harmonic Generation," Phys. Rev. Lett. **104**(20), 207402 (2010).
3. Y. Zhang, A. Manjavacas, N. J. Hogan, L. Zhou, C. Ayala-Orozco, L. Dong, J. K. Day, P. Nordlander, and N. J. Halas, "Toward Surface Plasmon-Enhanced Optical Parametric Amplification (SPOPA) with Engineered Nanoparticles: A Nanoscale Tunable Infrared Source," Nano Letters **16**(5), 3373–3378 (2016).
4. F. Timpu, A. Sergeyev, N. R. Hendricks, and R. Grange, "Second-Harmonic Enhancement with Mie Resonances in Perovskite Nanoparticles," ACS Photonics **4**(1), 76–84 (2017).
5. M. R. Shcherbakov, D. N. Neshev, B. Hopkins, A. S. Shorokhov, I. Staude, E. V. Melik-Gaykazyan, M. Decker, A. A. Ezhov, A. E. Miroshnichenko, I. Brener, A. A. Fedyanin, and Y. S. Kivshar, "Enhanced Third-Harmonic Generation in Silicon Nanoparticles Driven by Magnetic Response," Nano Letters **14**(11), 6488–6492 (2014).
6. D. Smirnova, A. I. Smirnov, and Y. S. Kivshar, "Multipolar second-harmonic generation by Mie-resonant dielectric nanoparticles," Physical Review A **97**(1), 013807 (2018).

7. I. Shoji, T. Kondo, A. Kitamoto, M. Shirane, and R. Ito, "Absolute scale of second-order nonlinear-optical coefficients," J. Opt. Soc. Am. B, JOSAB **14**(9), 2268–2294 (1997).
8. H. P. Wagner, M. Kühnelt, W. Langbein, and J. M. Hvam, "Dispersion of the second-order nonlinear susceptibility in ZnTe, ZnSe, and ZnS," Physical Review B **58**(16), 10494 (1998).
9. S. Bergfeld and W. Daum, "Second-Harmonic Generation in GaAs: Experiment versus Theoretical Predictions of χ_{xyz} (2)," Physical Review Letters **90**(3), 036801 (2003).
10. K. Pedersen, C. Fisker, and T. G. Pedersen, "Second-harmonic generation from ZnO nanowires," physica status solidi (c) **5**(8), 2671–2674 (2008).
11. M. Lafrentz, D. Brunne, A. V. Rodina, V. V. Pavlov, R. V. Pisarev, D. R. Yakovlev, A. Bakin, and M. Bayer, "Second harmonic generation spectroscopy of excitons in ZnO," Physical Review B **88**(23), 235207 (2013).
12. D. Staedler, T. Magouroux, R. Hadji, C. Joulaud, J. Extermann, S. Schwung, S. Passemard, C. Kasparian, G. Clarke, M. Gerrmann, and others, "Harmonic nanocrystals for biolabeling: a survey of optical properties and biocompatibility," Acs Nano **6**(3), 2542–2549 (2012).
13. P. Pantazis, J. Maloney, D. Wu, and S. E. Fraser, "Second harmonic generating (SHG) nanoprobes for in vivo imaging," PNAS **107**(33), 14535–14540 (2010).
14. E. Slenders, H. Bové, M. Urbain, Y. Mugnier, A. Y. Sonay, P. Pantazis, L. Bonacina, P. Vanden Berghe, M. vandeVen, and M. Ameloot, "Image Correlation Spectroscopy with Second Harmonic Generating Nanoparticles in Suspension and in Cells," The Journal of Physical Chemistry Letters **9**(20), 6112–6118 (2018).
15. L. Dubreil, I. Leroux, M. Ledevin, C. Schleder, L. Lagalice, C. Lovo, R. Fleurisson, S. Passemard, V. Kilin, S. Gerber-Lemaire, M.-A. Colle, L. Bonacina, and K. Rouger, "Multi-harmonic Imaging in the Second Near-Infrared Window of Nanoparticle-Labeled Stem Cells as a Monitoring Tool in Tissue Depth," ACS Nano **11**(7), 6672–6681 (2017).
16. F. Ramos-Gomes, W. Möbius, L. Bonacina, F. Alves, and M. A. Markus, "Bismuth Ferrite Second Harmonic Nanoparticles for Pulmonary Macrophage Tracking," Small 1803776 (2018).
17. K. Clays and A. Persoons, "Hyper-Rayleigh scattering in solution," Phys. Rev. Lett. **66**(23), 2980–2983 (1991).
18. F. W. Vance, B. I. Lemon, and J. T. Hupp, "Enormous Hyper-Rayleigh Scattering from Nanocrystalline Gold Particle Suspensions," J. Phys. Chem. B **102**(50), 10091–10093 (1998).
19. M. Jacobsohn and U. Banin, "Size Dependence of Second Harmonic Generation in CdSe Nanocrystal Quantum Dots," J. Phys. Chem. B **104**(1), 1–5 (2000).
20. A. Deniset-Besseau, J. Duboisset, E. Benichou, F. Hache, P.-F. Brevet, and M.-C. Schanne-Klein, "Measurement of the Second-Order Hyperpolarizability of the Collagen Triple Helix and Determination of Its Physical Origin," J. Phys. Chem. B **113**(40), 13437–13445 (2009).
21. J. Campo, F. Desmet, W. Wenseleers, and E. Goovaerts, "Highly sensitive setup for tunable wavelength hyper-Rayleigh scattering with parallel detection and calibration data for various solvents," Opt. Express, OE **17**(6), 4587–4604 (2009).
22. J. Campo, W. Wenseleers, E. Goovaerts, M. Szablewski, and G. H. Cross, "Accurate Determination and Modeling of the Dispersion of the First Hyperpolarizability of an Efficient Zwitterionic Nonlinear Optical Chromophore by Tunable Wavelength Hyper-Rayleigh Scattering," The Journal of Physical Chemistry C **112**(1), 287–296 (2008).
23. J. Campo, A. Painelli, F. Terenziani, T. Van Regemorter, D. Beljonne, E. Goovaerts, and W. Wenseleers, "First Hyperpolarizability Dispersion of the Octupolar Molecule Crystal Violet: Multiple Resonances and Vibrational and Solvation Effects," Journal of the American Chemical Society **132**(46), 16467–16478 (2010).
24. H. Linnenbank, Y. Grynko, J. Förstner, and S. Linden, "Second harmonic generation spectroscopy on hybrid plasmonic/dielectric nanoantennas," Light: Science & Applications **5**(1), e16013 (2016).
25. S. Winter, M. Zielinski, D. Chauvat, J. Zyss, and D. Oron, "The Second Order Nonlinear Susceptibility of Quantum Confined Semiconductors—A Single Dot Study," J. Phys. Chem. C **115**(11), 4558–4563 (2011).
26. S. Schwung, A. Rogov, G. Clarke, C. Joulaud, T. Magouroux, D. Staedler, S. Passemard, T. Jüstel, L. Badie, C. Galez, J. P. Wolf, Y. Volkov, A. Prina-Mello, S. Gerber-Lemaire, D. Rytz, Y. Mugnier, L. Bonacina, and R. L. Dantec, "Nonlinear optical and magnetic properties of $BiFeO_3$ harmonic nanoparticles," Journal of Applied Physics **116**(11), 114306 (2014).
27. N. Van Steerteghem, K. Clays, T. Verbiest, and S. Van Cleuvenbergen, "Third-Harmonic Scattering for Fast and Sensitive Screening of the Second Hyperpolarizability in Solution," Analytical Chemistry **89**(5), 2964–2971 (2017).
28. R. Le Dantec, Y. Mugnier, G. Djanta, L. Bonacina, J. Extermann, L. Badie, C. Joulaud, M. Gerrmann, D. Rytz, J. P. Wolf, and C. Galez, "Ensemble and Individual Characterization of the Nonlinear Optical Properties of ZnO and $BaTiO_3$ Nanocrystals," J. Phys. Chem. C **115**(31), 15140–15146 (2011).
29. C. Joulaud, Y. Mugnier, G. Djanta, M. Dubled, J.-C. Marty, C. Galez, J.-P. Wolf, L. Bonacina, and R. Le Dantec, "Characterization of the nonlinear optical properties of nanocrystals by Hyper Rayleigh Scattering," Journal of Nanobiotechnology **11**(Suppl 1), S8 (2013).
30. J. D. Jackson, *Classical Electrodynamics, 3rd ed*. (Wiley, 1999).
31. F. L. Huyskens, P. L. Huyskens, and A. P. Persoons, "Solvent dependence of the first hyperpolarizability of p-nitroanilines: Differences between nonspecific dipole–dipole interactions and solute–solvent H-bonds," The Journal of Chemical Physics **108**(19), 8161–8171 (1998).
32. D. Mohanty, G. S. Chaubey, A. Yourdkhani, S. Adireddy, G. Caruntu, and J. B. Wiley, "Synthesis and piezoelectric response of cubic and spherical $LiNbO_3$ nanocrystals," RSC Advances **2**(5), 1913–1916 (2012).

33. C. Xu, J. B. Shear, and W. W. Webb, "Hyper-Rayleigh and Hyper-Raman Scattering Background of Liquid Water in Two-Photon Excited Fluorescence Detection," Analytical Chemistry **69**(7), 1285–1287 (1997).
34. S. Kedenburg, M. Vieweg, T. Gissibl, and H. Giessen, "Linear refractive index and absorption measurements of nonlinear optical liquids in the visible and near-infrared spectral region," Optical Materials Express **2**(11), 1588-1611 (2012).
35. D. E. Zelmon, D. L. Small, and D. Jundt, "Infrared corrected Sellmeier coefficients for congruently grown lithium niobate and 5 mol% magnesium oxide –doped lithium niobate," Journal of the Optical Society of America B **14**(12), 3319-3322 (1997).
36. R. S. Klein, G. E. Kugel, A. Maillard, K. Polgár, and A. Péter, "Absolute non-linear optical coefficients of $LiNbO_3$ for near stoichiometric crystal compositions," Optical Materials **22**(2), 171–174 (2003).
37. B. Knabe, K. Buse, W. Assenmacher, and W. Mader, "Spontaneous polarization in ultrasmall lithium niobate nanocrystals revealed by second harmonic generation," Phys. Rev. B **86**(19), 195428 (2012).
38. J. L. Oudar and D. S. Chemla, "Hyperpolarizabilities of the nitroanilines and their relations to the excited state dipole moment," The Journal of Chemical Physics **66**(6), 2664–2668 (1977).
39. R. Bhatt, I. Bhaumik, S. Ganesamoorthy, A. K. Karnal, M. K. Swami, H. S. Patel, and P. K. Gupta, "Urbach tail and bandgap analysis in near stoichiometric $LiNbO_3$ crystals," physica status solidi (a) **209**(1), 176–180 (2012).
40. M. C. Larciprete and M. Centini, "Second harmonic generation from ZnO films and nanostructures," Applied Physics Reviews **2**(3), 031302 (2015).
41. J. C. Johnson, H. Yan, R. D. Schaller, P. B. Petersen, P. Yang, and R. J. Saykally, "Near-Field Imaging of Nonlinear Optical Mixing in Single Zinc Oxide Nanowires," Nano Lett. **2**(4), 279–283 (2002).
42. V. V. Multian, J. Riporto, M. Urbain, Y. Mugnier, G. Djanta, S. Beauquis, C. Galez, V. Y. Gayvoronsky, and R. Le Dantec, "Averaged third-order susceptibility of ZnO nanocrystals from Third Harmonic Generation and Third Harmonic Scattering," Optical Materials **84**, 579–585 (2018).
43. G. Clarke, A. Rogov, S. McCarthy, L. Bonacina, Y. Gun'ko, C. Galez, R. Le Dantec, Y. Volkov, Y. Mugnier, and A. Prina-Mello, "Preparation from a revisited wet chemical route of phase-pure, monocrystalline and SHG-efficient $BiFeO_3$ nanoparticles for harmonic bio-imaging," Scientific Reports **8**, 10473 (2018).
44. T. Tytus, O. Phelan, M. Urbain, G. Clarke, J. Riporto, R. Le Dantec, G. Djanta, S. Beauquis, V. Monnier, Y. Chevolot, C. Galez, and Y. Mugnier, "Preparation and Preliminary Nonlinear Optical Properties of $BiFeO_3$ Nanocrystal Suspensions from a Simple, Chelating Agent-Free Precipitation Route," Journal of Nanomaterials **2018**, 3019586 (2018).
45. R. Prasanth, L. K. van Vugt, D. A. M. Vanmaekelbergh, and H. C. Gerritsen, "Resonance enhancement of optical second harmonic generation in a ZnO nanowire," Applied Physics Letters **88**(18), 181501 (2006).
46. S. J. Clark and J. Robertson, "Band gap and Schottky barrier heights of multiferroic $BiFeO_3$," Appl. Phys. Lett. **90**(13), 132903 (2007).
47. R. C. Miller, "Optical second harmonic generation in piezoelectric crystals," Appl. Phys. Lett. **5**(1), 17–19 (1964).
48. J. Seres, "Dispersion of second-order nonlinear optical coefficient," Applied Physics B: Lasers and Optics **73**(7), 705–709 (2001).
49. V. Srikant and D. R. Clarke, "On the optical band gap of zinc oxide," Journal of Applied Physics **83**(10), 5447–5451 (1998).
50. S. G. Choi, H. T. Yi, S.-W. Cheong, J. N. Hilfiker, R. France, and A. G. Norman, "Optical anisotropy and charge-transfer transition energies in $BiFeO_3$ from 1.0 to 5.5 eV," Physical Review B **83**(10), (2011).
51. E. Luppi and V. Véniard, "A review of recent theoretical studies in nonlinear crystals: towards the design of new materials," Semiconductor Science and Technology **31**(12), 123002 (2016).